J|A|C|S
A R T I C L E S

Published on Web 10/06/2010

Molecular Insights into the Potential and Temperature Dependences of the Differential Capacitance of a Room-Temperature Ionic Liquid at Graphite Electrodes

Jenel Vatamanu, Oleg Borodin,* and Grant D. Smith

Department of Materials Science and Engineering, University of Utah, Salt Lake City, Utah 84112, United States

Received May 27, 2010; E-mail: Oleg.Borodin@utah.edu

Abstract: Molecular dynamics simulation studies of the structure and the differential capacitance (DC) for the ionic liquid (IL) *N*-methyl-*N*-propylpyrrolidinium bis(trifluoromethane)sulfonyl imide ([pyr$_{13}$][TFSI]) near a graphite electrode have been performed as a function temperature and electrode potential. The IL exhibits a multilayer structure that extends 20−30 Å from the electrode surface. The composition and ion orientation in the innermost layer were found to be strongly dependent on the electrode potential. While at potentials near the potential of zero charge (PZC), both cations and anions adjacent to the surface are oriented primarily perpendicular to the surface, the counterions in first layer orient increasingly parallel to the surface with increasing electrode potential. A minimum in DC observed around -1 V$_{RPZC}$ (potential relative to the PZC) corresponds to the point of highest density of perpendicularly aligned TFSI near the electrode. Maxima in the DC observed around $+1.5$ and -2.5 V$_{RPZC}$ are associated with the onset of “saturation”, or crowding, of the interfacial layer. The asymmetry of DC versus electrode polarity is the result of strong interactions between the fluorine of TFSI and the surface, the relatively large footprint of TFSI compared to pyr$_{13}$, and the tendency of the propyl tails of pyr$_{13}$ to remain adsorbed on the surface even at high positive potentials. Finally, an observed decreased DC and the disappearance of the minimum in DC near the PZC with increasing temperature are likely due to the increasing importance of entropic/excluded volume effects (interfacial crowding) with increasing temperature.

Introduction

Recent experimental[1−6] and theoretical[7−13] studies of the behavior of room-temperature ionic liquids (RTILs) have been stimulated by their enormous potential as electrolytes in energy storage devices[14,15] and alternative energy devices.[16−21] Practical applications of RTILs include, among others, electrostatic and electrochemical supercapacitors,[22,23] lithium batteries,[24−29] hydrogen fuel cells,[30−33] and solar cells.[34] The behavior of RTILs at charged interfaces is of paramount importance in these applications, particularly those that take advantage of the electrolyte structure to store energy. Here, the structure and capacitance of the electrode/electrolyte interface, commonly referred to as the electric double layer (EDL), and how the EDL capacitance depends upon electrode potential, RTIL chemical structure, electrode−electrolyte interactions, electrode geometry, and temperature are of great interest.

The dependence of the differential capacitance (DC) on the electrode potential and temperature are of particular interest, as they provide valuable information regarding the electrode−electrolyte interfacial behavior. Experiments have demonstrated that, close to the potential of zero charge (PZC), the DC for RTILs can exhibit a maximum[35−38] or a minimum,[39−42] depending upon the particular electrode material, the specific RTIL, and the temperature.[43−48] Experiments on systems having a relatively wide electrochemical window revealed complex camel-shaped DC for both RTILs and aqueous solutions of salts, consisting of a minimum near PZC flanked by two maxima, with decreasing wings of DC at larger positive or negative electrode potentials. In 2007, Kornyshev[13] pointed out that the traditional Gouy−Chapman−Stern model cannot predict a maximum at PZC observed for dense ionic liquids and offered a mean-field theory (MFT) that takes into account constrains imposed by ion packing. The MFT predicted a maximum of DC close to PZC, together with asymmetric DC behavior when cations and anions are different sizes, in good agreement with results of molecular dynamics (MD) simulations.[8] Modified

---

(1) Chmiola, J.; Yushin, G.; Gogotsi, Y.; Portet, C.; Simon, P.; Taberna, P. L. *Science* **2006**, *313*, 1760.
(2) Largeot, C.; Portet, C.; Chmiola, J.; Taberna, P. L.; Gogotsi, Y.; Simon, P. *J. Am. Chem. Soc.* **2008**, *130*, 2730.
(3) Simon, P.; Gogotsi, I. *Nat. Mater.* **2008**, *7*, 845.
(4) Cyr, M. D.; Venkataraman, B.; Flynn, G. W.; Black, A.; Whitesides, G. M. *J. Phys. Chem.* **1996**, *100*, 13747.
(5) Tao, F.; Bernasek, S. L. *J. Am. Chem. Soc.* **2005**, *127*, 12750.
(6) Su, Y.-Z.; Fu, Y.-C.; Yan, J.-W.; Chen, Z.-B.; Mao, B.-W. *Angew. Chem., Int. Ed.* **2009**, *48*, 5148.
(7) Pei, Y.; Ma, J. *J. Am. Chem. Soc.* **2005**, *127*, 6802.
(8) Fedorov, M. V.; Kornyshev, A. A. *J. Phys. Chem. B* **2008**, *112*, 11868.
(9) Kislenko, S. A.; Samoylov, I. S.; Amirov, R. H. *Phys. Chem. Chem. Phys.* **2009**, *11*, 5584.
(10) Dong, K.; Ahou, G.; Liu, X.; Yao, X.; Shang, S.; Lyubartsev, A. *J. Phys. Chem. C.* **2009**, *113*, 10013.
(11) Sieffert, N.; Wipff, G. *J. Phys. Chem. C.* **2008**, *112*, 19590.
(12) Goel, T.; Patra, N. C.; Ghosh, K. S.; Mukherjee, T. *J. Chem. Phys.* **2008**, *129*, 154707.
(13) Kornyshev, A. A. *J. Phys. Chem. B* **2007**, *111*, 5545.
(14) Pandolfo, A. G.; Hollemkamp, A. F. *J. Power Sources* **2006**, *157*, 11.
(15) Yang, C. M.; Kim, Y.-J.; Endo, M.; Kanoh, H.; Yudasaka, M.; Iijima, S.; Kaneko, K. *J. Am. Chem. Soc.* **2007**, *129*, 20.

Poisson−Boltzmann (MPB) theory and atomistic simulations reported by Lamperski et al.[49] revealed that a maximum in DC at the PZC (leading to the so-called bell-shaped behavior of DC) is promoted by high density and high thermal energy (given as the ratio of *kT* and the electrostatic energy for ions in close contact). In contrast, low density and low thermal energy promote a minimum in DC near the PZC, leading to the so-called U-shaped DC. The transition from U-shaped to bell-shaped behavior with increasing density and/or thermal energy was associated with increasingly important packing constraints at the electrode interface. Higher ion density in the bulk electrolyte clearly leads to higher ion density at the interface and the onset of excluded volume interactions at lower electrode potentials, while higher thermal energy increases the importance of entropic penalties for packing/ordering of ions at the electrolyte/electrolyte interface. Since "saturation" of the interface (see discussion below) eventually occurs with increasing electrode potential, even for low-density/low-thermal-energy electrolytes, at high enough electrode potentials the DC begins to decrease with further increase in electrode potential, even for systems that exhibit U-shaped behavior. This leads to the so-called camel-shaped behavior, i.e., a minimum in DC near the PZC, flanked by maxima at positive and negative electrode potentials.

While complex dependence of the DC on electrode potential is observed in simple spherical models, indicating that complex molecular structure is not needed to produce camel-shaped DC, it is clear that the *specific* behavior of a given RTIL/electrode combination depends upon the details of the molecular structure of the ions, the ion−substrate interactions, and the temperature. For example, it has been recently illustrated[13] that a region of U-shaped DC is possible only if there are sufficient empty sites on the electrode surface. Furthermore, it has been found[50] that polarizability effects, modeled as a distance-dependent dielectric constant, can promote camel-shaped DC. Inclusion of dispersion interaction between ions and between ions and the surface, which were ignored in the majority of simulation studies, also significantly influences the behavior of DC.[51] For example, including dispersion interactions between ions results in the appearance of camel-shaped DC for the model RTIL that showed only a maximum in simulations without inclusion of these interactions.[51] The depth of the camel-shaped capacitance minimum near zero surface potential was also significantly influenced by the ion−surface dispersion interactions.[51] Finally, recent modeling studies[52,53] show that the presence of neutral tails promotes U-shaped/camel-shaped DC behavior, as the neutral tails appear to play the role of latent voids that can be replaced by charged counterions. The larger the tails, the more pronounced the camel-shaped behavior becomes.[53]

To date, the majority of simulation studies of RTIL DC as a function of electrode voltage have focused on simple models designed to represent generic features of RTILs. While a number of simulation studies of atomistic RTILs such as [1-ethyl-3-methylimidazolium][NO_3][54] and [1-butyl-3-methylimidazolium][PF_6][55] between flat surfaces and [tetraethylammonium][BF_4] in a carbon nanotube forest[56] have been reported, only the first study[54] reported on the dependence of DC on the potential drop across EDLs applied over a limited potential range (−1.8 to 0.9 V). In the simulation study presented here, we investigate the EDL structure and DC for *N*-methyl-*N*-propylpyrrolidinium bis(trifluoromethane)sulfonyl imide ([pyr_{13}][TFSI]) at a graphite electrode using atomistic MD simulations as a function of electrode potential (−3.5 to 3.5 V) and temperature. The [pyr_{13}][TFSI] RTIL was chosen instead of the popular imidazolium-based RTILs due to a wider electrochemical window of the former that will translate into higher energy

---

(16) Anderson, J. L.; Armstrong, D. W.; Wei, G.-T. *Anal. Chem.* **2006**, 2893.
(17) Hapiot, P.; Lagrost, C. *Chem. Rev.* **2008**, *108*, 2238.
(18) Parsons, R. *Chem. Rev.* **1990**, *90*, 813.
(19) Schmickler, W. *Chem. Rev.* **1996**, *96*, 3177.
(20) McCreery, R. L. *Chem. Rev.* **2008**, *108*, 2646.
(21) Kötz, R.; Press, M. C. *Electrochim. Acta* **2000**, *45*, 2483.
(22) Conway, B. E. *Electrochemical Capacitors: Scientific Fundamentals and Technological Applications*; Kluwer: Dordrecht, The Netherlands, 1999.
(23) Arico, A. S.; Bruce, P.; Scrosati, B.; Tarascon, J.-M.; Schalkwijk, W. V. *Nat. Mater.* **2005**, *4*, 366.
(24) Seki, S.; Kobayashi, Y.; Miyashiro, H.; Ohno, Y.; Usami, A.; Mita, Y.; Kihira, N.; Watanabe, M.; Terada, N. *J. Phys. Chem. C* **2009**, *113*, 6596.
(25) Fuller, J.; Carlin, R. T.; Osteryoung, R. A. *J. Electrochem. Soc.* **1997**, *144*, 3881.
(26) Castriota, M.; Caruso, T.; Agostino, R. G.; Cazzanelli, E.; Henderson, W. A.; Passerini, S. *J. Phys. Chem. A* **2005**, *109*, 92.
(27) Hayashi, K.; Nemoto, Y.; Akuto, K.; Sakurai, Y. *J. Power Sources* **2005**, *146*, 689.
(28) Garcia, B.; Lavallée, S.; Perron, G.; Michot, C.; Armand, M. *Electrochim. Acta* **2004**, *49*, 4583.
(29) Sato, T.; Maruo, T.; Marukane, S.; Takagi, K. *J. Power Sources* **2004**, *138*, 253.
(30) Souza, R F.; Padilha, J. C.; Gonçalves, R. S.; Dupont, J. *Electrochem. Commun.* **2003**, *5*, 728.
(31) Hagiwara, R.; Nohira, T.; Matsumoto, K.; Tamba, Y. *Electrochem. Solid States Lett.* **2005**, *8*, A321.
(32) Dupont, J.; de Souza, R. F.; Suarez, P. A. Z. *Chem. Rev.* **2002**, *102*, 3667.
(33) Noda, A.; Susan, M. A. B. H.; Kudo, K.; Mitsushima, S.; Hayamizu, K.; Watanabe, M. *J. Phys. Chem. B* **2003**, *107*, 4024.
(34) Bai, Y.; Cao, Y.; Zhang, J.; Wang, M.; Li, R.; Wang, P.; Shaik, M.; Zakeeruddin, S. M.; Grätzel, M. *Nature Mater.* **2008**, *7*, 626.
(35) Alam, M. T.; Islam, M. M.; Okijima, T.; Ohsaka, T. *J. Phys. Chem. C* **2009**, *113*, 6569.
(36) Paynem, R. *Trans. Faraday Soc.* **1965**, *61*, 316.
(37) Doubova, L. M.; Trasatti, S. *Condens. Matter Phys.* **2001**, *4*, 759.
(38) Langkau, T.; Baltruschat, H. *Electrochim. Acta* **2002**, *47*, 1595.
(39) Lockett, V.; Sedev, R.; Ralston, J.; Horne, M.; Rodopoulos, T. *J. Phys. Chem. C* **2008**, *112*, 7486.
(40) (a) Grahame, D. C. *J. Am. Chem. Soc.* **1954**, *76*, 4819. (b) Grahame, D. C. *J. Am. Chem. Soc.* **1956**, *79*, 2093.
(41) Islam, M. M.; Alam, M. T.; Okijima, T.; Oshaka, T. *J. Phys. Chem. C* **2009**, *113*, 3386.
(42) Islam, M. M.; Alam, M. T.; Okijima, T.; Oshaka, T. *Electrochem. Commun.* **2007**, *9*, 2370.
(43) Figueiredo, M.; Gomes, C.; Costa, R.; Martis, A.; Pereora, C. M.; Silva, F. *Electrochim. Acta* **2009**, *54*, 2630.
(44) Silva, F.; Gomes, C.; Figueiredo, M.; Renata, C.; Martins, A.; Pereira, C. M. *J. Electroanal. Chem.* **2008**, *662*, 153.
(45) Hills, G.; Silva, F. *Can. J. Chem.* **1981**, *59*, 1835.
(46) Hamelin, A.; Stoicoviciu, L.; Silva, F. *J. Electroanal. Chem.* **1987**, *229*, 107.
(47) Caprio, D.; Stafiej, J.; Borkowska, Z. *J. Electroanal. Chem.* **2005**, *582*, 41.
(48) Fawcett, W. R.; Borkowska, Z. *J. Phys. Chem.* **1983**, *87*, 4861.
(49) Lamperski, S.; Outhwaite, C. W.; Bhuiyan, L. B. *J. Phys. Chem. B* **2009**, *113*, 8925.
(50) Lauw, Y.; Horne, M. D.; Rodopoulos, T.; Leermarks, F. A. M. *Phys. Rev. Lett.* **2009**, *103*, 117801.
(51) Trulsson, M.; Algotsson, J.; Forsman, J.; Woodward, C. E. *J. Phys. Chem. Lett.* **2010**, *1*, 1191.
(52) Fedorov, M. V.; Georgi, N.; Kornyshev, A. A. *Electrochem. Commun.* **2010**, *12*, 296.
(53) Georgi, N.; Kornyshev, A. A.; Fedorov, M. V. *J. Electroanal. Chem.* **2010**, in press, corrected proof, doi: 10.1016/j.jelechem.2010.07.004.
(54) Feng, G.; Zhang, J. S.; Qiao, R. *J. Phys. Chem. C* **2009**, *113*, 4549.
(55) Kislenko, S. A.; Samoylov, I. S.; Amirov, R. H. *Phys. Chem. Chem. Phys.* **2009**, *11*, 5584.
(56) Yang, L.; Fishbine, B. H.; Migliori, A.; Pratt, L. R. *J. Am. Chem. Soc.* **2009**, *131*, 12373.

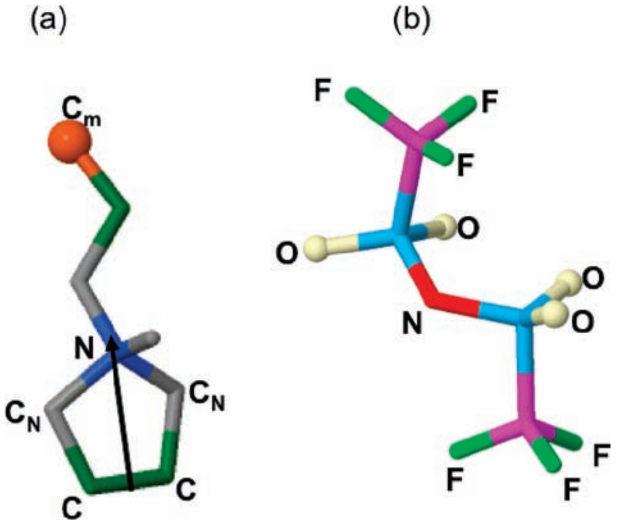

Figure 1. Illustration of united atom pyr_{13} cation (a) and all-atom TFSI anion (b). Atoms for which atomic density profiles are calculated are labeled. The arrow on pyr_{13} represents the ring vector utilized in determining the orientation of the cation with respect to the surface.

density,[57] as the energy density in supercapacitors is linearly proportional to capacitance and strongly depends on voltage (roughly quadratic, if the voltage dependence of capacitance is neglected). Unlike previous reports for [emim][NO_3]/flat surface simulations,[54] our simulations reveal that [pyr_{13}][TFSI] exhibits camel-shaped DC. MD simulations of this important RTIL have allowed us to gain insight into the complex DC and EDL structure for real (atomistic detailed) ionic liquids, including the effects of ion−surface interactions, ion shape, molecular orientation, and temperature on EDL behavior.

Simulation Details

In our simulations, the pyr_{13} cation was represented by a united atom model where hydrogen atoms are not explicitly considered, while the TFSI anion was represented by an all-atom model. The structures of the cation and anion are shown in Figure 1. The force field was fitted to optimize the bulk densities, heat of vaporization, and diffusion coefficient relative to [pyr_{13}][TFSI] properties extracted from our previous MD simulations using an all-atom polarizable model (APPLE&P force field) and experiments.[58−60] MD simulations using the APPLE&P accurately described RTIL liquid and crystal structure, conductivity, ion self-diffusion coefficients, and viscosity.[58−60] Development and validation of the united atom force field is described in the Supporting Information.

The simulations were performed on 113 [pyr_{13}][TFSI] ion pairs confined between graphite electrodes under constant and controlled potential difference between electrodes.[61,62] Each graphite electrode consisted of three graphene layers, with a cross section of 25.62 Å × 25.65 Å each. Rather than assuming a constant electrode charge, the electrode polarization was evaluated by minimizing the total electrostatic energy with respect to the electrode charges. The electrode charges were represented as Gaussian distributed,[63] having a width of 0.5 Å,[61,62] while the electrolyte charges were point charges. Figure S1 in the Supporting Information shows an image snapshot from the simulation trajectory at 393 K, along with the distance between electrodes. Additional details of this simulation methodology can be found in refs 61 and 62. The long-range interactions were evaluated using the SMPE Ewald technique for 2D periodic geometries.[64,65] The short-range interactions were evaluated over a spherical cutoff radius of 10 Å. The equations of motion were integrated with a time-reversible multiple-step algorithm[66] over time resolutions of 0.1 fs (bonds, bending angles, out-of-plane deformations), 0.5 fs (dihedrals and nonbonded short-range interactions within 7.5 Å cutoff), and 3.0 fs (longer-range nonbonded interactions including Fourier space part of SMPE). Electrode charges were evaluated every 30 fs including explicit evaluation of the Fourier part at every iteration.

For the purpose of this work, we chose temperatures of 453, 393, and 363 K, which are sufficiently high to require at most only several nanoseconds (2−4 ns) of equilibration and 24 ns of production run simulation for each individual trajectory. At 453 K, simulation trajectories were obtained for 28 applied voltages between electrodes, while at 393 and 363 K, trajectories were generated for 29 applied voltages between electrodes. At each applied voltage, the EDLs at the negative and positive electrodes were analyzed separately; thus, we report data for 56 EDLs at 453 K and 58 EDLs at 393 and 363 K. The distance between electrodes was adjusted to match [pyr_{13}][TFSI] density in the middle of the simulation cell from the 3D periodic bulk simulations at the same temperature and pressure of 1 atm. The statistics on EDL structure were collected every 30 fs over two sets of 12 ns simulations. The second set of 12 ns simulations was run to test the reproducibility of our results—both trajectories predicted similar results.

Results and Discussion

Differential Capacitance. We begin our analysis by studying DC as a function of EDL potential drop. The potential drop within the electric double layer, V_{EDL}, is defined as the difference between the electrode potential and the screened bulk potential, $V_{EDL} = V_{electrode} - V_{bulk}$. Since the potential of zero charge (PZC) is nonzero for our systems, it is convenient to set the potential scale V_{RPZC} as relative to potential of zero charge, $V_{RPZC} = V_{EDL} - PZC = V_{electrode} - V_{bulk} - PZC$. The PZC was approximated from the Poisson potential drop within the EDL at 0 V potential between the two electrodes. Values of PZC of −0.37, −0.34, and −0.41 V for temperatures 363, 393, and 453 K, respectively, were obtained. Negative PZC indicates a larger affinity of the uncharged electrode surface for the anions compared to cations. The relatively large negative PZC is due to the high density of negatively charged fluorine atoms of TFSI situated next to the uncharged graphite electrode, as discussed in detail below. The EDL potentials relative to PZC were found in the following ranges: from −3.40 to +3.30 V at 363 K, from −3.47 to +3.46 V at 393 K, and from −3.64 to +3.50 V at 453 K.

---

(57) Pringle, J. M.; Golding, J.; Baranyai, K.; Forsyth, C. M.; Deacon, G. B.; Scott, J. L.; MacFarlane, D. R. *New J. Chem.* **2003**, *27*, 1504.
(58) Borodin, O. *J. Phys. Chem. B* **2009**, *113*, 11463.
(59) Borodin, O.; Smith, G. D. *J. Phys. Chem. B* **2006**, *110*, 11481.
(60) Borodin, O.; Gorecki, W.; Smith, G. D.; Armand, M. *J. Phys. Chem. B* **2010**, *114*, 6786.
(61) Reed, S. K.; Lanning, O. J.; Madden, P. A. *J. Chem. Phys.* **2007**, *126*, 084704.
(62) Vatamanu, J.; Borodin, O.; Smith., G. D. *Phys. Chem. Chem. Phys.* **2010**, *12*, 183.
(63) Siepmann, J. I.; Sprik, M. *J. Chem. Phys.* **1995**, *102*, 511.
(64) (a) Heyes, D. M. *Phys. Rev. B: Condens. Matter* **1994**, *49*, 755. (b) Parry, D. E. *Surf. Sci.* **1975**, *49*, 433. (c) Heyes, D. M.; Barber, M.; Clarke, J. H. R. *J. Chem. Soc., Faraday Trans. 2* **1977**, *73*, 148. (d) Heyes, D. M. *J. Phys. Chem. Solids* **1980**, *41*, 291. (e) Heyes, D. M.; van Swol, F. *J. Chem. Phys.* **1981**, *75*, 5051. (f) Heyes, D. M. *J. Chem. Phys.* **1983**, *79*, 4010. (g) Heyes, D. M. *Phys. Rev. B: Condens. Matter* **1984**, *30*, 2182.
(65) (a) Kawata, M.; Mikami, M. *Chem. Phys. Lett.* **2001**, *340*, 157. (b) Kawata, M.; Nagashima, U. *Chem. Phys. Lett.* **2001**, *340*, 165. (c) Kawata, M.; Mikami, M.; Nagashima, U. *J. Chem. Phys.* **2002**, *116*, 3430. (d) Kawata, M.; Mikami, M.; Nagashima, U. *J. Chem. Phys.* **2002**, *117*, 3526. (e) Kawata, M.; Mikami, M.; Nagashima, U. *J. Chem. Phys.* **2001**, *115*, 4457.
(66) Tuckerman, X. M. E.; Berne, B. J.; Martyna, G. J. *J. Chem. Phys.* **1990**, *97*, 1990.

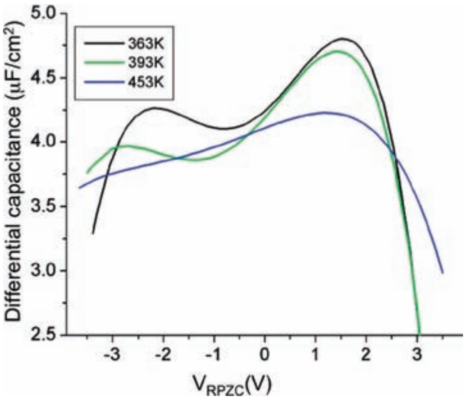

Figure 2. Differential capacitance as a function of electrode potential relative to the potential of zero charge.

The DC was determined as follows. First, the dependence of electrode charge density on V_{RPZC} was fitted with an order five polynomial utilizing all values of V_{RPZC} simulated. The DC as a function of V_{RPZC} was then obtained as the analytical derivative of the fitted polynomial. Shown in Figure 2 is the DC versus V_{RPZC} at the three simulation temperatures. Also shown in Figure S3 in the Supporing Information is the DC obtained from "local" fits involving fitting an order two polynomial over nine consecutive potential points. The DC from these local fits is in qualitative agreement with the DC shown in Figure 2, obtained from the global fits.

Figure 2 indicates that, at 363 and 393 K, the DC is camel-shaped, having a minimum shifted about −1 V from PZC and exhibiting saturation (maxima) around +1.5 and −2.5 V_{RPZC}. The magnitude of DC, around 4−4.8 μF/cm^2, is within the range observed in experiments for similarly sized ions.[67,68] For example, a maximum of DC at 8.7 μF/cm^2 was observed for [pyr$_{14}$][TFSI] at a Pt electrode at 298 K. As DC increases with decreasing temperature, a higher value of DC from experiments performed at 298 K is expected compared to the simulation value from 363 K.[68]

A steep decrease in DC is observed for large positive and negative electrode potentials, which is especially pronounced at the lowest simulation temperature. The maximum in DC on the positive electrode is greater than that at the negative one (Figure 2). It is interesting to note that the PZC in our simulations corresponds to neither a minimum nor a maximum in DC. While simple EDL theories predict a minimum in DC at PZC, experimental measurements of DC[35,40] clearly show that the position of the minimum or maximum in DC depends upon the particular system and often does not correspond to PZC.

Next we explore the temperature dependence of DC. The transition from camel-shaped to bell-shaped DC occurs at our highest temperature (453 K) as follows: the minimum in DC flattens out with increasing temperature and disappears at 453 K, while the maximum in DC at the positive potential is preserved (Figure 2). In agreement with experimental results,[45−47] we find that the location of the minimum and maximum in DC versus potential relative to PZC does not change with temperature. Our results show negative temperature dependence of DC at potentials near PZC (decreasing DC with increasing temperature). The negative DC slope observed at low voltages and the disappearance of the minimum near PZC with increasing temperature are consistent with the increasing importance of the entropic penalty paid by the electrolyte to structure near the electrode with increasing temperature (see discussion of simplified models above). This entropic penalty increases the free energy cost associated with increasing the charge/potential of the electrodes, thereby reducing the differential capacitance. Experiments have identified both positive and negative temperature dependence of DC. Positive temperature dependence of DC was observed for the RTIL [1-butyl-3-methylimidazolium][PF$_6$] on both Pt and graphite electrodes[44] and for imidazolium-based ILs as well.[69] Negative temperature dependence was observed for similar ILs and an Hg electrode,[70] as well as for molten salt electrolytes.[71] While Monte Carlo simulations,[72−74] modified MSA theory,[75] and DFT theory[76] have revealed that the DC can have both negative and positive temperature dependence for the restricted primitive model, a negative temperature dependence is expected for the density and temperature of our simulations.

Electric Double-Layer Structure. In agreement with recent simulations[53,61,62,77] and experimental observations[78] on ILs, we observe a multilayer structure extending 20−30 Å from the electrode surface in the profiles of molecular density, charge, integral charge, and Poisson potential as shown in Figure 3 for 393 K. Thus, electrolyte structuring extends to four to five electrolyte layers and becomes more pronounced with increasing surface potential. While at 0 V potential difference between electrodes, the densities and potential profiles are the same (within statistical uncertainty) at both electrodes, at large potentials we see an accumulation of the negative ion (TFSI) at the positive electrode and the positive ion (pyr$_{13}$) at the negative electrode, as expected. A smaller potential drop across the EDL and greater structure in the charge density profile are observed at the positive electrode compared to the negative electrode at 5.8 V applied potential difference. This is consistent with the behavior exhibited by the DC in Figure 2, where generally DC is larger for the positive electrode than for the negative electrode.

Figure 4 shows the center-of-mass density profiles for pyr$_{13}$ and TFSI as a function of position relative to the electrode surface near the electrode interface for various EDL potentials. It can be seen that the electrolyte forms well-defined layers near the substrate, with an innermost layer 4−5.3 Å from the interface, an intermediate layer 5.3−7.5 Å from the surface, and a second layer 7.5−9 Å from the surface. At potentials near the PZC, the cation and anion populate both the first and intermediate layers, with the majority of ion centers located in the intermediate layer. With increasing electrode potential (positive or negative), the co-ion (ions with the same charge as the electrode) population in the first layer decreases, and the

---

(67) Alam, M. T.; Islam, M.; Okajima, T.; Ohsaka, T. *J. Phys. Chem. C* **2008**, *112*, 16600.

(68) Islam, M.; Alam, M. T.; Ohsaka, T. *J. Phys. Chem. C* **2008**, *112*, 16568.

(69) Locket, V.; Sedev, R.; Ralston, J.; Horne, M.; Rodopoulos, T. *J. Phys. Chem. C* **2008**, *112*, 7486.

(70) Alam, M. T.; Islam, Md. M.; Okijima, T.; Ohsaka, T. *J. Phys. Chem. C* **2007**, *111*, 18326.

(71) Kisza, A. *Electrochim. Acta* **2006**, *51*, 2315.

(72) Boda, D.; Henderson, D.; Chan, K.-Y. *J. Chem. Phys.* **1999**, *110*, 5346.

(73) Bhuiyan, L. B.; Outhwaite, C. W.; Henderson, D. *J. Chem. Phys.* **2005**, *123*, 34704.

(74) Reszko-Zygmunt, J.; Sokolowski, S. *J. Chem. Phys.* **2005**, *123*, 16101.

(75) Holovsko, M.; Kapko, V.; Henderson, D.; Boda, D. *Chem. Phys. Lett.* **2001**, *341*, 363.

(76) Reszko-Zygmunt, J.; Sokolowski, S.; Henderson, D.; Boda, D. *J. Chem. Phys.* **2005**, *122*, 84504.

(77) Desai, T. G. *J. Chem. Phys.* **2007**, *127*, 154707.

(78) Baldelli, S. *Acc. Chem. Res.* **2008**, *41*, 421.

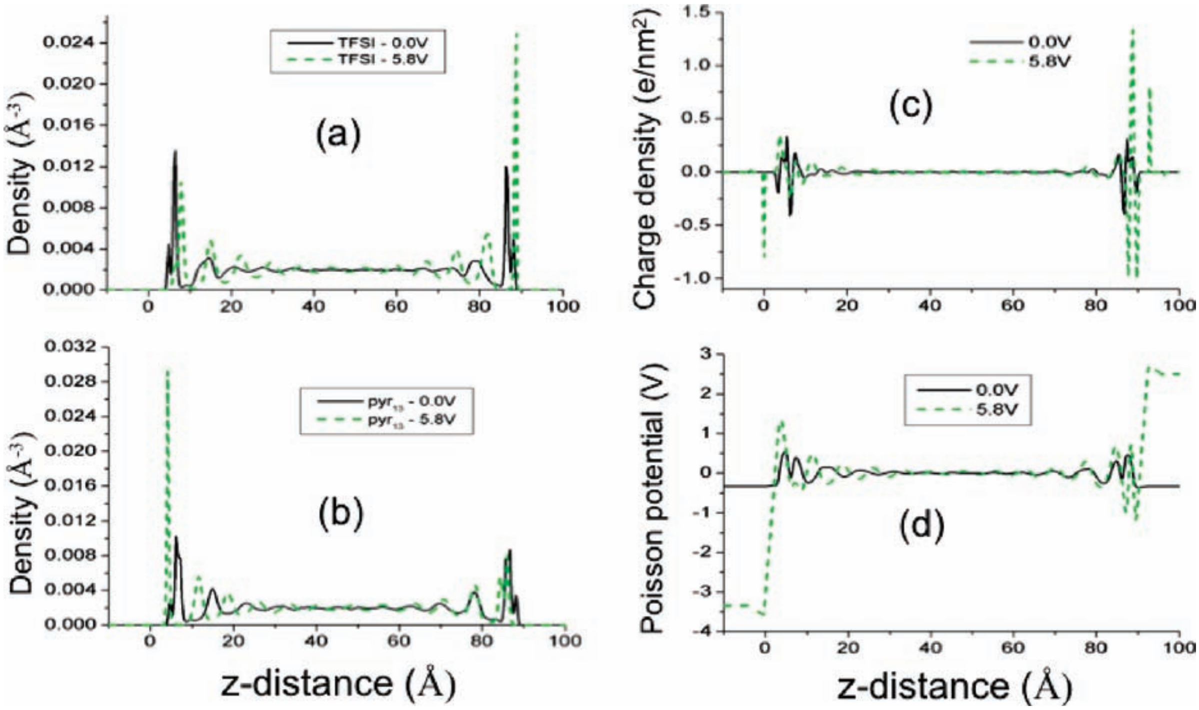

Figure 3. Profiles as a function of position relative to the electrode surface of (a) number density for the center-of-mass of TFSI, (b) number density for the center-of-mass of pyr_{13}, (c) charge density for a potential difference between electrodes of 0 and 5.8 V, and (d) Poisson potential, at a potential difference between electrodes of 0 and 5.8 V. The represented system was at 393 K.

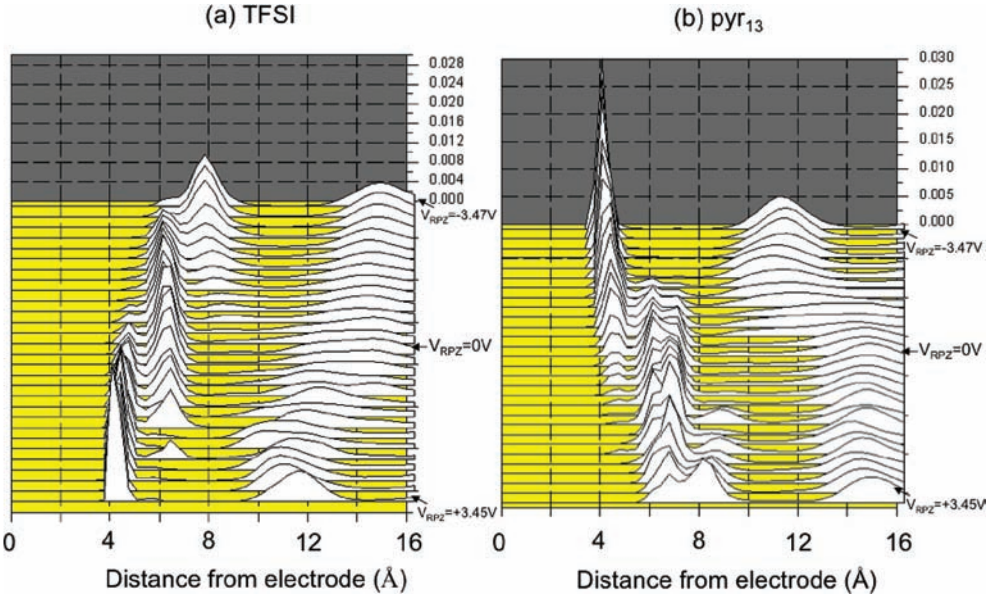

Figure 4. Ion center-of-mass density as a function distance from the electrode surface for a series of electrode potentials V_{RPZC} for (a) TFSI and (b) pyr_{13} at 393 K.

co-ion population in the intermediate layer initially increases up to approximately 1 V. Concurrently, the counterion population in the intermediate layer decreases, and the counterion population in the first layer increases. At large (positive or negative) electrode potentials, the density of co-ions in the intermediate layer decreases, and the co-ion population in the second layer increases. At the saturation potential (the potential where DC has a maximum), the first layer is dominated by counterions.

Relationship between DC and Interfacial Structure. In order to obtain a more detailed picture of the relationship between DC and [pyr_{13}][TFSI] interfacial structure as a function of the applied potential, we calculated the density profiles for atoms comprising pyr_{13} and TFSI ions as a function of electrode potential, shown in Figure 5, cumulative atomic and ion densities in the interfacial layers as a function of electrode potential, shown in Figure 6, and the orientational distribution functions for pyr_{13} and TFSI ions with respect to the substrate for three V_{RPZ} values, shown in Figure 7. The orientational distribution is calculated for the TFSI anion using the angle between the surface normal and a vector connecting the two carbon atoms in TFSI, while the angle between the surface normal and the ring vector are used for pyr_{13}, as shown in Figure 1. These orientational distributions were weighted with the corresponding

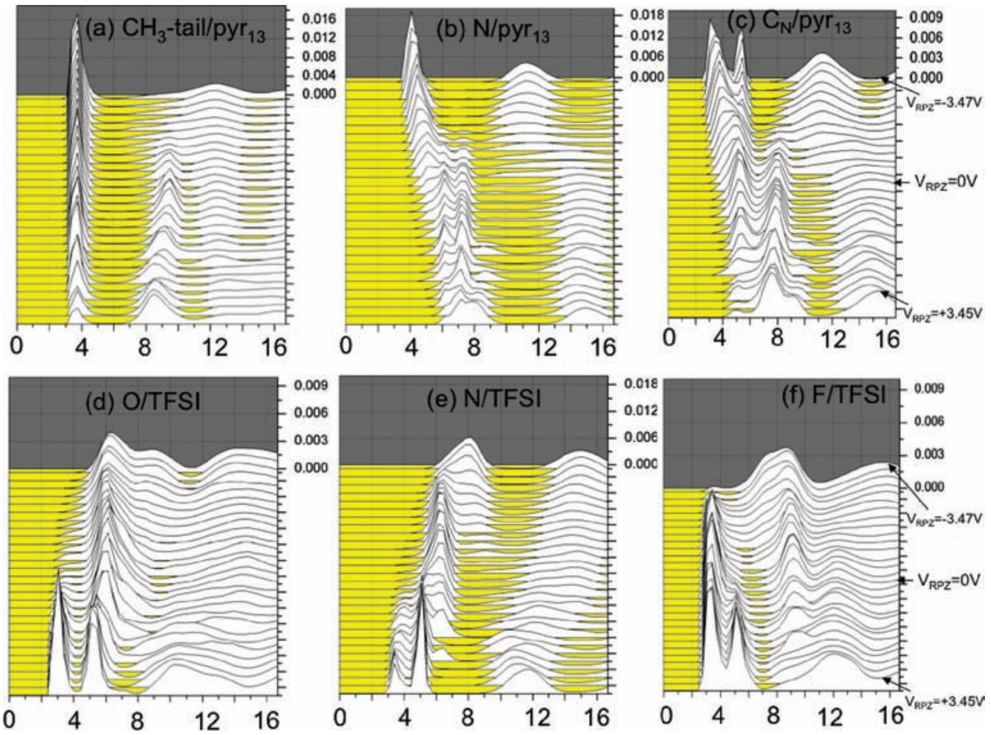

Figure 5. Atom number density (in Å^{-3}) as a function of distance (x-axis in Å) for the electrode surface for a series of electrode potentials V_{RPZC} and for (a) CH_3 group of the propyl tail, (b) pyr_{13} nitrogen atom, (c) pyr_{13} C_N atoms, (d) TFSI oxygen atoms, (e) TFSI nitrogen atom, and (f) TFSI fluorine atoms. The density profiles were divided by the number of atoms of each type in the ion pair.

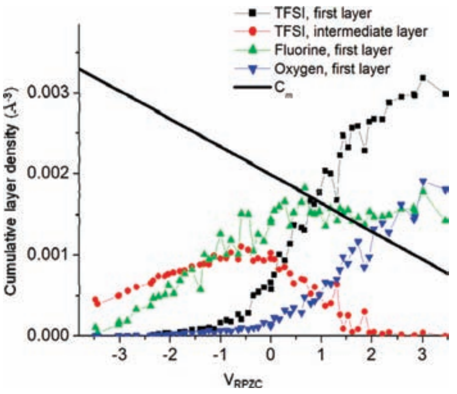

Figure 6. Cumulative density profiles (averaged within a layer) for TFSI center-of-mass, TFSI oxygen atoms, TFSI fluorine atoms, and pyr_{13} propyl end groups as a function of electrode potential at 393 K. The propyl end group density is shown as a linear fit in electrode potential in order to simplify the figure. The density profiles were divided by the number of atoms of each type in the ion pair to make their scales similar.

ion population to reflect ion orientation in the overall interfacial layer. For the cumulative atomic and ion densities, we have considered the first layer to correspond to 0−5.3 Å from the interface and the intermediate layer 5.3−7.5 Å from the surface, as observed for the ion center-of-mass density profiles. For the ion orientation analysis, we have divided the ions into layers on the basis of their center-of-mass position relative to the substrate, with the first layer being 0−5.3 Å from surface, the second 5.3−7.5 Å from the surface, and the third 10−14 Å from the surface. The distributions of orientations are shown for ions in each layer at electrode potentials of 0, −3.47 (cation), and +3.45 V_{RPZC} (anion). Figure 8 provides representative snapshots illustrating ion packing at different applied potentials.

Shown in Figure 5 is the density profile for CH_3 groups from the propyl tail of pyr_{13} (a), the positively charged nitrogen atom of pyr_{13} (b), and the density of the carbon atoms of the pyr_{13} ring bonded to the nitrogen atom (c), as denoted in Figure 1. The density profiles for the fluorine (d) and highly negatively charged nitrogen (e) and oxygen atoms (f) of TFSI are also shown. According to Figure 5, at the PZC, the inner electrolyte layer is occupied largely by the propyl tail of pyr_{13} (essentially nonpolar) and the fluorine atoms of the TFSI (small negative charge), with a significant population of C carbons of the pyr_{13} ring (not shown in Figure 5; see Figure 1 for labels). These groups with the relatively small charge could be seen as "latent voids" in the light of recent modeling work using simplified models.[53] There are relatively few highly charged TFSI oxygen and nitrogen atoms or pyr_{13} N or C_N atoms in the inner layer, and the ion center-of-mass density is greater in the intermediate layer than in the first layer (see Figure 4). As V_{RPZC} becomes increasingly negative, the number of TFSI anions with their center-of-mass in the inner layer disappears, as shown in Figures 4 and 6, and we observe an increase in TFSI in the intermediate layer until around −1 V_{RPZC}. In this range (0 to −1 V_{RPZC}), Figures 5 and 6 show that the density of relatively large fluorine atoms on the substrate remains constant, while Figure 2 shows a decrease in DC in this potential range. The electrode is becoming increasingly crowded as the density of positively charged pyr_{13} rings increases and the fluorine atom density remains roughly constant in this range of potentials. At larger negative potentials, TFSI ions are pushed away from the surface, as can be seen in the increasing population of TFSI in the second layer (Figure 4) and the decreasing population of fluorine atoms on the substrate (Figures 5b and 6), yielding an alignment as shown in Figure 8b, allowing more space for pyr_{13} rings to occupy the surface. Simultaneously, the center-of-mass density of pyr_{13} in the inner layer increases and the population in the intermediate layer disappears, with increasingly large negative potentials, as shown in Figure 4. The density of C_N and N from pyr_{13} in the first layer also increases dramatically with increasing negative potential

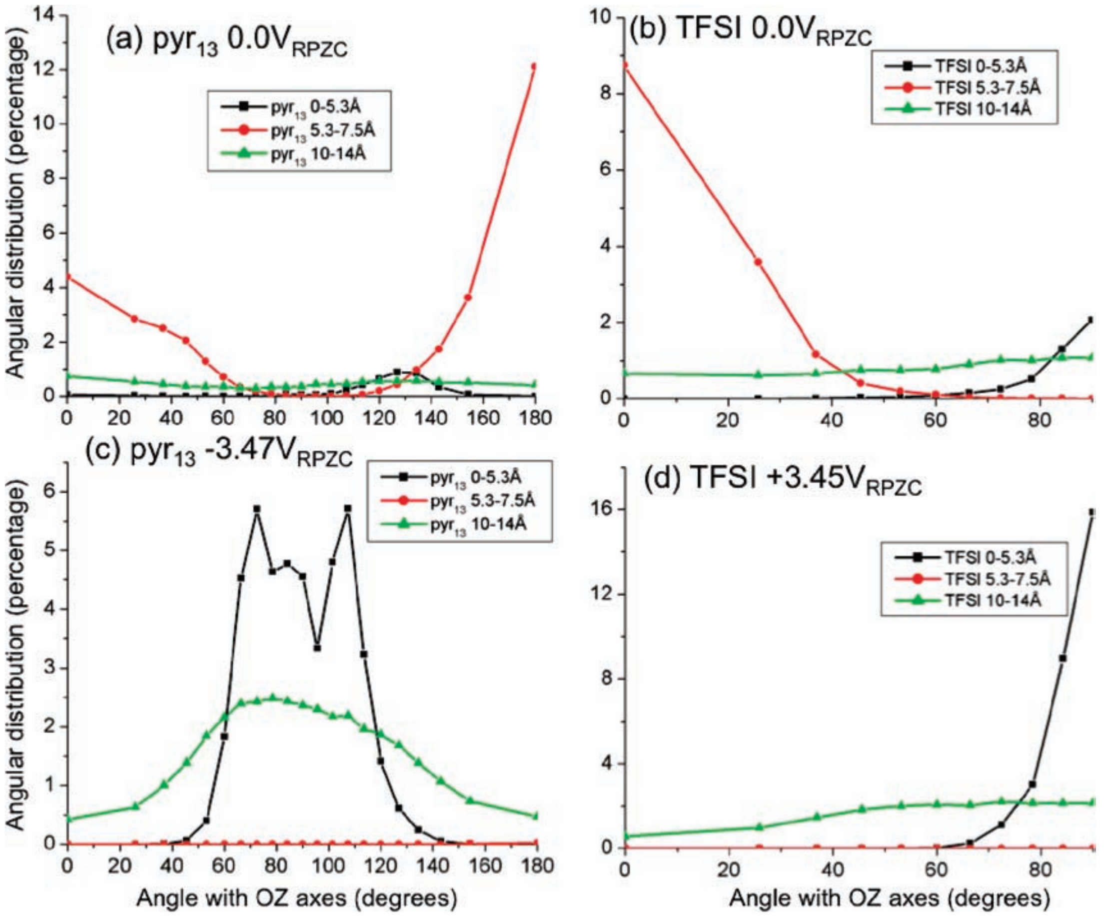

Figure 7. Distribution of angles between the surface normal vector and the vector connecting the center of the C−C bond and N atom of pyr$_{13}$ (see Figure 1) and the vector connecting the C atoms of TFSI multiplied by the probability of finding ions in the first (0−5.3 Å), second (5.3−7.5 Å), or third (10−14 Å) layer from simulations at 393 K. (a,b) At PZC; (c) −3.47 V$_{RPZC}$; and (d) +3.45 V$_{RPZC}$.

(Figure 5), consistent with the pyr$_{13}$ ring rotating from being perpendicular to the surface at PZC to parallel to the surface, as shown in Figures 7 (first layer distributions) and 8. This results in a decrease in the footprint of the pyr$_{13}$ molecule, allowing for a relatively high packing density before the onset of saturation effects. These occur at potentials (and associated electrode charge densities) more negative than about −2.5 V$_{RPZC}$. Interestingly, the density of C$_m$ (propyl tail) increases slightly as the potential becomes more negative up to −3.5 V$_{RPZC}$, in contrast with observations from the coarse-grained IL simulations[53] with one and two neutral beads attached to the charge bead, in which the neutral groups became depleted from the first layer as the potential became more negative, with most of the neutral beads being situated in the second layer already at −1.6 V$_{RPZC}$. Thus, at negative electrode potentials less than −1.6 V$_{RPZC}$, pyr$_{13}$'s are oriented parallel to the electrode, as shown in Figure 8, while for the coarse-grained[53] IL with two neutral beads, the cations are oriented perpendicular to the surface for the same potential range. We speculate that propyl tails will eventually shift from the first interfacial layer to the second layer, but we expect this to happen at much more negative potentials than investigated in this work.

The observed reorientation of pyr$_{13}$ at the interface with increasing V_{RPZC} seems to correlate with the experimental evidence for 1-ethyl-3-methylimidazolium (emim$^+$) cation orientation deduced from FT-IR[79] and in situ surface-enhanced infrared absorption spectroscopy.[80] In line with our observations, Nanbu et al.[79,80] concluded that emim$^+$ cations present in the interphase orient vertically, or at least not parallel, with the methyl or ethyl groups of emim$^+$ directed toward the surface in a potential range of −1.3 to +0.6 V vs Ag|Ag$^+$ and parallel to the surface at large negative potentials. MD simulations[81] of [emim][FSI] at LiFePO$_4$ surfaces also showed largely perpendicular orientation of emim$^+$ cations to the surface for uncharged electrodes, in contrast to the imidazolium rings oriented parallel to the surface found in [bmim][TFSI] simulations at α-Quartz-(001).[11]

As V_{RPZC} becomes increasingly positive from 0 V$_{RPZC}$, Figure 5 reveals a dramatic increase in the population of highly negatively charged TFSI oxygen atoms. At the same time, Figure 6 reveals that the density of large fluorine atoms in the inner layer remains roughly constant, while the population of TFSI in the intermediate layer decreases, reaching very low levels around 1.5 V$_{RPZC.}$ The split-peak structure of the oxygen and fluorine density profiles allows us to assign a parallel arrangement of TFSI at the highly positively charged surface as shown in Figure 8, which is confirmed by calculations of the orientational distribution function shown in Figure 7. Note, that, with increasing V_{RPZC}, the population of pyr$_{13}$ propyl end groups remains reasonably high, even at the highest positive potentials,

---

(79) Nanbu, N.; Sasaki, Y.; Kitamura, F. *Electrochem. Commun.* **2003**, *5*, 383.

(80) Nanbu, N.; Kato, T.; Sasaki, Y.; Kitamura, F. *Electrochemistry* **2005**, *73*, 610.

(81) Smith, G. D.; Borodin, O.; Russo, S. P.; Rees, R. J.; Hollenkamp, A. F. *Phys. Chem. Chem. Phys.* **2009**, *11*, 9884.

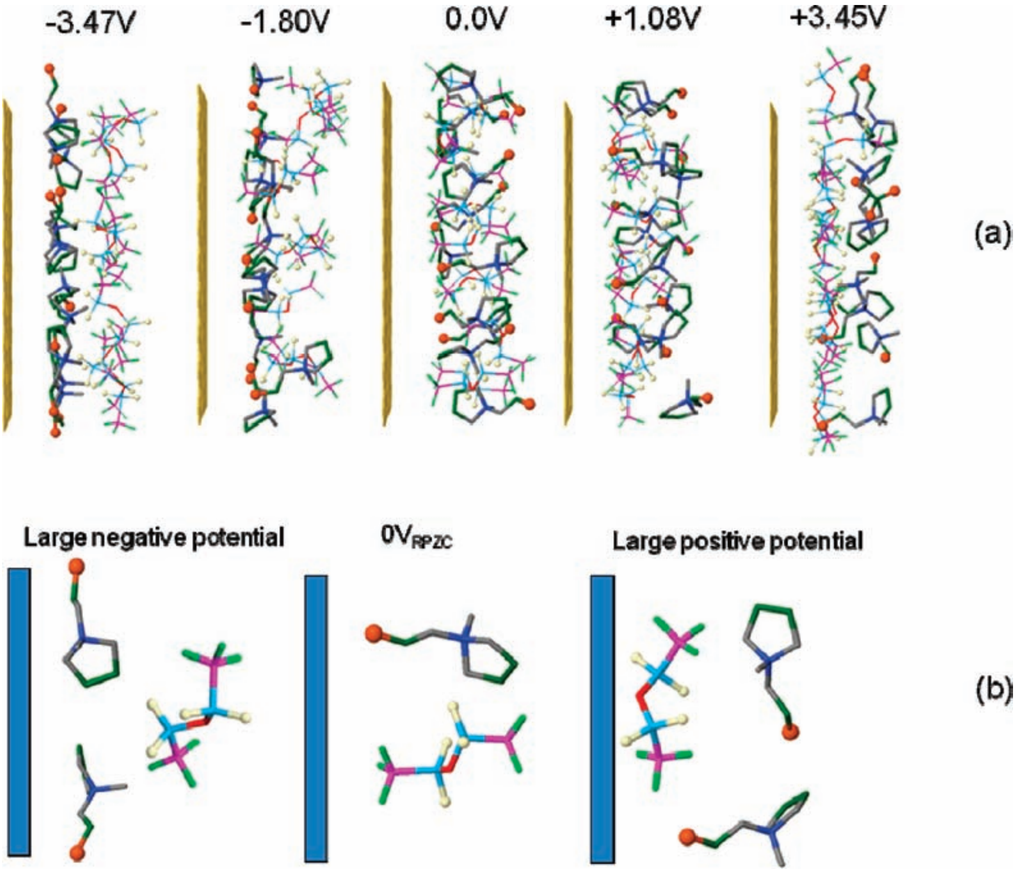

Figure 8. (a) Snapshot images of ions near the electrode at different potentials relative to the potential of zero charge. (b) Scheme illustrating changes of ion orientations with applied potential.

when most pyr$_{13}$ center-of-mass moved out from the innermost layer to the intermediate and outer layers. Additionally, Figure 4 shows that the pyr$_{13}$ center-of-mass population in the intermediate layer remains appreciable even at the highest positive potential. The faster saturation of DC observed on the positive electrode (around 1.5 V$_{RPZC}$) compared to the negative electrode (around −2.5 V$_{RPZC}$) is likely the result of the relatively large footprint of TFSI compared to pyr$_{13}$ and the larger (by ∼10 kJ/mol) magnitude of the negative nonbonded energy of TFSI on the positive electrode compared the nonbonded energy of pyr$_{13}$ on the negative electrode as measured at 2 V potential difference applied between electrodes. In the potential range from 0 to +1.5 V$_{RPZC}$, the DC increases rapidly with increasing electrode potential, indicating that adsorption of TFSI oxygen atoms on the surface is occurring easily and brings highly charged oxygen atoms close to the surface, forming a highly compact and charged inner-layer open reorientation from perpendicular to parallel to the surface. However, at +1.5 V$_{RPZC}$, most TFSI anions in the interface have reoriented, and further increase of negative charge requires bringing new TFSI anions to the already crowded interface. Part of this crowding comes from the remaining propyl tails of the pyr$_{13}$ cations, whose center-of-mass occupies the intermediate layer even at high positive potentials. Representative snapshots of pyr$_{13}$ and TFSI orientations at high positive potentials are shown in Figure 8a, and a schematic representation of changes in ion orientations near the electrode, versus potential, is shown in Figure 8b.

Ion Orientation as a Function of Separation from the Substrate. Analysis of pyr$_{13}$ and TFSI orientation as a function of the distance from the electrode surface shown in Figure 7 indicates that orientational correlations attenuate significantly as ions get farther from the surfaces, moving beyond 10 Å from the electrode. Simulations also reveal that, at distances farther than 20 Å from the surface, the orientational distributions are flat for both TFSI and pyr$_{13}$, indicating random orientation of ions. Note that the angular distribution functions shown in Figure 7 were multiplied by the corresponding probability of finding ions in each layer from the three layers considered here in order to indicate the relative importance of each layer and their contributions to the overall interfacial orientation. Figure 7 shows that, at PZC, the ions closest to the interface have their orientation constrained to either a 30° tilt with the surface plane for innermost pyr$_{13}$ or parallel to the surface for innermost TFSI; however, this innermost layer is only sparsely populated. The ions in the most populated layer at PZC, the intermediate layer (within 5.3−7.5 Å from the surface), are oriented perpendicular to the graphite surface. Thus, at PZC, the overall ion orientation within 7.5 Å is characterized by ratios of perpendicular to parallel (or tilted) of 3.4:1 for TFSI and 8.4:1 for pyr$_{13}$, supporting the notion that, at PZC, most ions near the interface are oriented perpendicular to the surface. A closer look at the pyr$_{13}$ orientations in the intermediate layer at 0 V$_{RPZC}$ reveals a higher probability of finding the pyr$_{13}$ vector (see Figure 1) around 180° than around 0° with our ZO axes, as shown in Figure 7a; therefore, the preference is for pyr$_{13}$ to be oriented with the propyl tail toward the surface, as represented in Figure 8b.

The TFSI ions from the intermediate layer are also oriented mostly perpendicular to the surface (Figure 7b), and in this orientation the end-group CF_3 of TFSI in the intermediate can penetrate to the electrode surface. This results in a large fluorine atom density at the surface, even for zero electrode charge and the corresponding negative PZC. Increasing the positive potential toward saturation, the TFSI ions became oriented parallel to the surface, exposing the more charged O toward the surface. Interestingly, this parallel structuring propagates to the second and third layers. Figure 7 also demonstrates that the reorientations of pyr_{13} cations located within 7.5 Å of the surface changes from predominantly perpendicular to parallel to the surface, bringing highly charged groups (N and C_N) closer to the surface as the potential increases to -3.47 V_{RPZC}. Interestingly, not only does pyr_{13} within 7.5 Å of the surface rotate from being perpendicular to parallel to the surface with decreasing V_{RPZC} from 0 to -3.5 V, but this behavior is mimicked by pyr_{13} in the outmost interfacial layer (10−14 Å).

Differential Capacitance at Large Positive and Negative Electrode Potentials. The double-layer model of Kornyshev[13] predicted, on the basis of the conservation of charge principle, that the DC decays at large potentials as $C \propto |U|^{-0.5}$, and accordingly, the electrode charge density increases at $|\sigma| \propto |U|^{0.5}$. Such a behavior is considered a typical signature of lattice saturation, where no more ions can be packed near the surface, and therefore it is the thickness of the double layer that can grow in order to accumulate sufficient ions within EDLs in order to compensate the increasing charge on the electrode.[82] These theoretical predictions were found to be in very good agreement with MD simulation results using a simple model of spherical ions.[8,53,83] Simulations using repulsive ions with 2:1 ratios of ion sizes clearly showed $C \propto |U|^{-0.5}$ limiting behavior for negative potentials[8] and for the restricted model,[83] while the exponent for the limiting behavior for positive potentials for the model with 2:1 ratios of ion sizes could not be unambiguously extracted from simulations data from our point of view, especially in the region below 7 V.[8] In a very recent paper published while ours was in revision, Georgi et al.[53] verified that $C \propto |U|^{-0.5}$ behavior occurs from potentials as low as 0.7 V for simple systems consisting of charged and neutral tails and experimentally for the alkylimidazolium chloride ILs.

We investigated the behavior of DC for positive electrode potentials[84] from our simulations and found a slower than $|U|^{0.5}$ increase of electrode charge (which means a faster than $|U|^{-0.5}$ decrease of DC) for a surprisingly large window of potential beyond maxima in DC. Specifically, in the EDL potential range $1.7 < U < 3.5$ V_{RPZC}, which corresponds to decaying wings of DC at the positive electrode, we found the exponents α between -0.6 and -0.8 for $C \propto |U|^{\alpha}$, as shown in Figure S4 in the Supporting Information. Our observations are in accord with the DC behavior reported in the self-consistent mean-field theory study of an IL having a dendrimeric structure.[50] The dendrimeric RTIL yielded $\alpha = -0.6$ and -0.8 for $C \propto |U|^{\alpha}$, with α being dependent on the effective dielectric constant. The slower than $|\sigma| \propto |U|^{0.5}$ increase in electrode charge indicates that rearrangements within EDLs are still possible beyond the DC maximum (confirmed indeed by our density profiles), and the free energy penalty required to bring an ion from bulk to an already crowded electrode is slightly larger than the free energy required for $L_{eff} \propto |U|^{0.5}$ growth of the effective double-layer thickness of a saturated lattice. It is important, however, to note that our preliminary simulations of a similar RTIL, $[pyr_{13}]$[bis(fluorosulfonyl)imide], indicate that $\alpha = -0.5$ limiting behavior is indeed observed, albeit at higher potentials, suggesting that, in the range from -3.5 to 3.5 V, the limiting behavior has not been yet reached for $[pyr_{13}]$[TFSI] due to conformational and reorientational changes still occurring in the first interfacial layer with increasing potential.

Conclusions

Atomistic MD simulations of $[pyr_{13}]$[TFSI] in contact with graphite electrodes performed as a function of electrode potential have allowed us to establish a clear connection between changes in the ion structure near the interface and the behavior of DC with changing electrode potential. Our simulations reveal that ion shape and reorientation are as important as changes in ion density in determining the behavior of DC with electrode potential. In particular, we would point out that, while pyr_{13} has a slightly larger volume than TFSI, it can (and does) align on the substrate, reducing its effective size on the substrate and apparently allowing for high charge density before saturation effects are manifested on the negative electrode. The lower value of DC at saturation on the negative electrode (albeit at a larger potential relative to the PZC) may reflect a relatively high density of the uncharged pyr_{13} propyl tails and ring C atoms situated near the graphite surface, while at the point of DC saturation on the positive electrode, only a small fraction of pyr_{13} propyl tails are present at the interface, with highly charged TFSI oxygen atoms forming the innermost layer very close to the graphite surface. One can say that pyr_{13} charge is located in the center of the molecule and is screened from strong interaction with the surface and other pyr_{13} cations, while TFSI oxygen atoms are located on the outside of the anion, allowing formation of the compact charge layer very close to the graphite surface but having a strong repulsion with other TFSI anions, leading to the larger effective footprint. The larger TFSI footprint compared to pyr_{13}, together with the stronger interaction energy in the first layer, results in saturation at the positive electrode at relatively low potentials compared to the saturation at the negative electrode. We also note that the saturation regime where $C \propto |U|^{-0.5}$ has not been reached within -3.5 to 3.5 V relative to the PZC potential window of our simulations.

Acknowledgment. The authors are grateful to U.S. Department of Energy under contract grant DE-SC0001912 to the University of Utah. The united atom force field development was supported by the U.S. Air Force Office of Scientific Research, Department of the Air Force, contract number FA9550-09-C-0110, to Wasatch Molecular Inc. and the University of Utah. Discussions with Doug Henderson, Ian Burgess, Yuri Gogotsi, and Wesley Henderson are highly appreciated.

Supporting Information Available: Development and validation of the united atom force field, a picture of the simulation cell, and surface charge vs double potential. This material is available free of charge via the Internet at http://pubs.acs.org.

JA104273R

---

(82) According to ref 13, the increase with potential of the effective double layer, L_{eff}, with the applied potential, given by $L_{eff} \propto |U|^{0.5}$, is equivalent to the conservation of electric charge for saturated surfaces.

(83) Fedorov, M. V.; Kornyshev, A. A. *Electrochim. Acta* **2008**, *53*, 6835.

(84) We concentrated on the limiting behavior of DC for positive electrode potentials because more data points are available for the electrode potential beyond double-layer saturation compared to the negative electrode.